Appl. Math. Mech. -Engl. Ed., **42**(5), 689–702 (2021)

APPLIED MATHEMATICS AND MECHANICS (ENGLISH EDITION)

https://doi.org/10.1007/s10483-021-2715-7

Mechanics of nonbuckling interconnects with prestrain for stretchable electronics*

Zixuan LU[1,2], Liang GUO[1,†], Hongyu ZHAO[1,2,†]

1. State Key Laboratory of Nonlinear Mechanics, Institute of Mechanics, Chinese Academy of Sciences, Beijing 100190, China;
2. School of Engineering Science, University of Chinese Academy of Sciences, Beijing 100049, China

(Received Oct. 19, 2020 / Revised Jan. 8, 2021)

Abstract The performance of the flexibility and stretchability of flexible electronics depends on the mechanical structure design, for which a great progress has been made in past years. The use of prestrain in the substrate, causing the compression of the transferred interconnects, can provide high elastic stretchability. Recently, the nonbuckling interconnects have been designed, where thick bar replaces thin ribbon layout to yield scissor-like in-plane deformation instead of in- or out-of-plane buckling modes. The nonbuckling interconnect design achieves significantly enhanced stretchability. However, combined use of prestrain and nonbuckling interconnects has not been explored. This paper aims to study the mechanical behavior of nonbuckling interconnects bonded to the prestrained substrate analytically and numerically. It is found that larger prestrain, longer straight segment, and smaller arc radius yield smaller strain in the interconnects. On the other hand, larger prestrain can also cause larger strain in the interconnects after releasing the prestrain. Therefore, the optimization of the prestrain needs to be found to achieve favorable stretchability.

Key words nonbuckling interconnect, prestrain, finite deformation, stretchability, stretchable electronics

Chinese Library Classification O343
2010 Mathematics Subject Classification 74K10, 74S05, 74B05

1 Introduction

Flexible electronics with a rapid development in recent years have broken through the limitation of traditional rigid electronic devices, and have brought the emergence of flexible display[1–2] and bendable mobile phones[3]. In addition, flexible electronics technology has also expanded further applications of electronic devices in medicine[4–5], energy[6], aerospace, and bionics[7–8], especially in epidermal electronics[9], wearable devices[10], and implantable devices[4–11].

Mechanical structure design is used in flexible electronics to realize the flexibility and stretchability and to make sure that the silicon and metal materials inside the device undergo negligible

* Citation: LU, Z. X., GUO, L., and ZHAO, H. Y. Mechanics of nonbuckling interconnects with prestrain for stretchable electronics. *Applied Mathematics and Mechanics* (*English Edition*), **42**(5), 689–702 (2021) https://doi.org/10.1007/s10483-021-2715-7

† Corresponding authors, E-mails: guoliang@imech.ac.cn, zhaohongyu@imech.ac.cn

deformations (<1% strain)[12–13]. Based on this characteristic, the circuit prepared on the plane can be transferred to any non-expandable surface and still has deformability during the use of the device[14–16]. The stretchable structures, the key of the flexible and stretchable electronics, have experienced a rapid evolution. It began when the buckling of thin metal films was found on polydimethylsiloxane (PDMS) substrates with prestrain[17], and this "wavy" structure was successfully implemented with silicon in experiments with overall stretchability less than 10%[12]. The "wavy" structure was further extended to a two-dimensional structure, which produced complex three-dimensional buckling configurations through biaxial prestretching[18]. Then, the island-bridge layout, in which the active components are mounted at the islands and the electrical circuit interconnects form the bridges, was developed as a popular approach to achieve stretchable properties[7,9,17–20]. This provides further possibilities for achieving functional flexible electronic devices. For instance, the island-bridge layout was transferred to the ball through the transfer printing technology and yielded hemispherical electronic eye cameras[7]. The structural designs for interconnects have evolved from straight to curvilinear layouts[21–22], from those fully bonded to or embedded in the elastomer substrates[23] to free-standing configuration[24–25], and from simple[21] to self-similar designs[6,26–29], which yield greater stretchability. Corresponding theoretical models such as the thin film interconnect with thickness variation[30] and buckled ribbons under out-of-plane loading promise the diverse design of stretchable electronics[31]. Zhang et al.[32] introduced the application of prestrain strategy together with interconnects in narrow serpentine shapes, which yielded significantly enhanced stretchability. They showed that interconnects fully bonded to the elastomeric substrate yielded in- or out-plane deformation after releasing the prestrain. Several experiments were carried out and proved the enhancement of systematic stretchability for different sets of electronic materials and geometrical parameters.

Different from the out-of-plane buckling for thin structures (metals, insulators, or semiconductors with thickness typically between 100 nm and 1 μm approximately, much smaller than its width), a nonbuckling interconnect design was introduced, where thick beam-liked bar replaced the thin ribbon interconnect[29]. The nonbuckling interconnect shows a scissor-like in-plane deformation instead of in- or out-of-plane buckling and provides enhanced stretchability, low resistance, and easiness for encapsulation compared with the traditional buckling layout design. Liu et al.[33] systematically studied the mechanical and electrical behaviors of nonbuckling interconnect design compared with buckling design and gave an analytic model for its finite deformation problem.

To further enhance the stretchability of the interconnect design, this work combines the prestrain strategy and the nonbuckling serpentine interconnect design. An analytic finite deformation model is given and confirmed by finite element analysis (FEA) results in Section 2. Different sets of relevant factors including the levels of prestrain and geometrical parameters are considered in Section 3. Concluding remarks are given in Section 4. This work is a key for providing the guidelines for nonbuckling interconnect design of stretchable electronics with prestrain.

2 Analytic model for nonbuckling interconnect with prestrain strategy

A schematic illustration of the nonbuckling interconnects with the use of prestrain strategy is shown in Fig. 1. Bonded onto a stretched substrate, the beam-like serpentine interconnect is subjected to compression and possesses in-plane deformation after releasing the prestrain, which configures it into a form with enhanced stretchability. In this section, an analytic model for the finite deformation problem of the nonbuckling serpentine interconnect design with prestrain is developed. Accurate deformation configurations after releasing the prestrain and under stretching of the serpentine interconnects are obtained. The relationships on non-dimensional maximum strain of the interconnect component versus levels of prestrain and structural design are

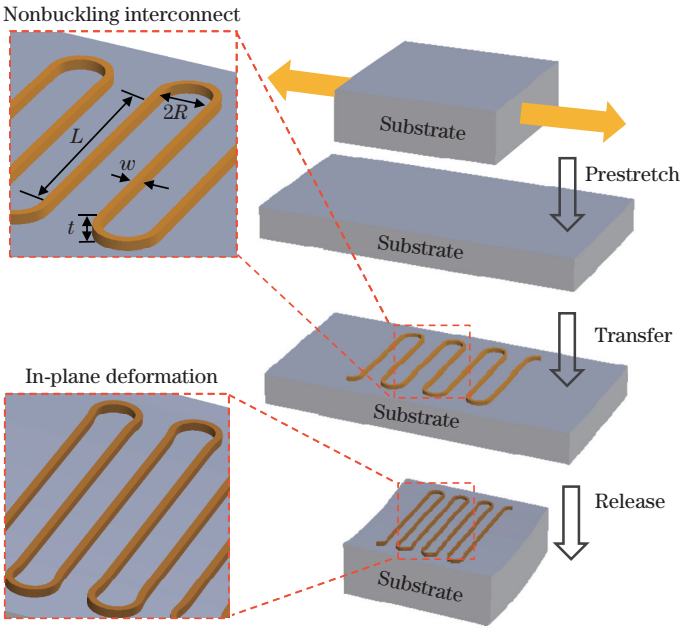

Fig. 1 Schematic illustration of prestrain strategy to substrate with fully bonded serpentine nonbuckling interconnect layout and its nonbuckling deformation after releasing prestrain (color online)

also discussed.

Releasing of the prestrain in the substrate leads to an average compression in the interconnects, which yields pure in-plane bending because of the nonbuckling design. The compressed nonbuckling structure can be regarded as an in-plane curve beam subjected to horizontal compression or stretching. Figure 2(a) illustrates the serpentine interconnects with multiple periods under compression. Considering the symmetry, Fig. 2(b) shows a quarter period of the serpentine interconnect in the undeformed state (before releasing the prestrain), the compressed configuration (after releasing the prestrain), and the stretched configuration. Remarkably, the right end A is an inflection point and supports free rotation and displacement on the x-axis. The left end C is guided, allowing only vertical displacement along the y-axis without rotation. R and L are the radius of the arc part and the length of the straight-line segment, respectively. A horizontal force P is applied on A due to the compression after releasing the prestrained substrate or stretching based on the elastic theory[34],

$$EI\Delta\kappa = M, \tag{1}$$

where EI is the flexural rigidity of the structure, with E being Young's modulus and I being the moment of inertia of the cross section, $\Delta\kappa$ is the increment of the local curvature (inverse of curvature radius), and M is the bending moment.

Based on the coordinate system in Fig. 2(b), we have $\Delta\kappa = |\frac{\mathrm{d}(\theta-\theta_0)}{\mathrm{d}s}|$, where θ and θ_0 are the angles between the x-axis and the tangent directions at a point of deformed or undeformed configurations correspondingly; s is the curvilinear coordinate, denoting the distance along the axis of the curved structure from point A. Combining this condition with Eq. (1), we get

$$EI\left|\frac{\mathrm{d}\,(\theta-\theta_0)}{\mathrm{d}s}\right| = Py. \tag{2}$$

Since

$$\frac{\mathrm{d}^2\theta_0}{\mathrm{d}s^2} = 0, \quad \frac{\mathrm{d}y}{\mathrm{d}s} = \sin\theta,$$

we can organize those following equations by simply making derivative and integration from Eq. (2). In the case of the uncertainness of relationship between θ and $\pi/2$, however, Eq. (2) should be integrated to remain positive at all time for both sides, which yields

$$\frac{1}{2}EI\left(\frac{\mathrm{d}\theta}{\mathrm{d}s}\right)^2 = -P|\cos\theta| + C. \tag{3}$$

The analytic models of the nonbuckling interconnects in the compressed configuration (shown in the middle of Fig. 2(b)) and in the stretched configuration (shown on the right side of Fig. 2(b)) are discussed, respectively.

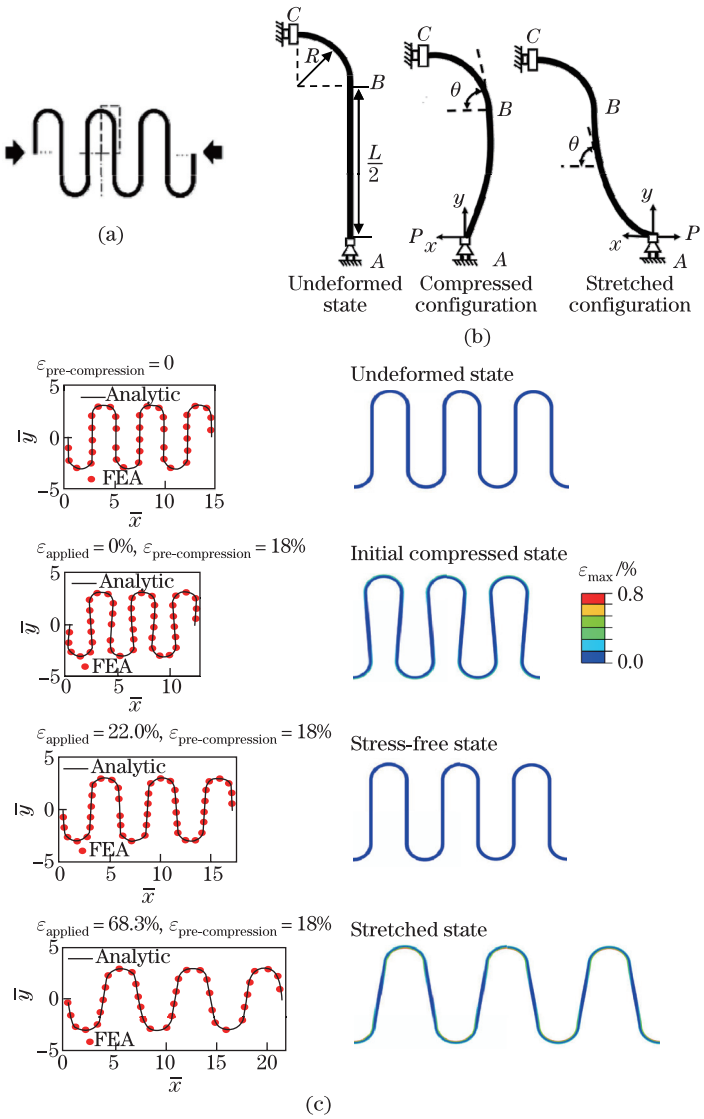

Fig. 2 (a) Serpentine interconnects with multiple periods under compressing. (b) Quarter period of interconnect in different states: undeformed state (before releasing prestrain of substrate), compressed configuration (after releasing prestrain), and stretched configuration (under significant stretching). (c) Comparison of configurations between analytic model and FEA and corresponding distribution of maximum principal strain for interconnect without substrate (color online)

In the compressed configuration, for AB part, the conditions of $\theta > \pi/2$ and $\cos\theta < 0$ yield

$$\frac{1}{2}EI\Big(\frac{\mathrm{d}\theta}{\mathrm{d}s}\Big)^2 = P\cos\theta + C, \tag{4}$$

where C is the constant which can be specified by the boundary condition. For BC part, the uncertainness of the relationship between θ and $\pi/2$ makes the equation remain to be Eq. (3).

For AB part, the boundary condition at point A possesses $\frac{\mathrm{d}\theta}{\mathrm{d}s} = 0$ and $\theta > \pi/2$, because A is an inflection point and should be jointed to another quarter period, which gives $C = -P\cos\theta_A$, where θ_A is the angle between the x-axis and the tangent at point A in the deformed configuration. $\frac{\mathrm{d}\theta}{\mathrm{d}s} < 0$ in AB part gives $\mathrm{d}s = -\mathrm{d}\theta/\sqrt{2P\left(\cos\theta - \cos\theta_A\right)/(EI)}$ from Eq. (4). A length constraint of AB part gives

$$\frac{L}{2} = \int_0^{L/2}\mathrm{d}s = -\int_{\theta_A}^{\theta_B}\frac{1}{\sqrt{\dfrac{2P}{EI}\left(\cos\theta - \cos\theta_A\right)}}\mathrm{d}\theta, \tag{5}$$

where θ_B is the angle between the x-axis and the tangent at point B in the deformed configuration. The coordinates of a point in AB part can be obtained as follows:

$$\begin{cases} x = \displaystyle\int_0^s \cos\theta\mathrm{d}s = -\int_{\theta_A}^{\theta_B}\frac{\cos\theta}{\sqrt{\dfrac{2P}{EI}\left(\cos\theta - \cos\theta_A\right)}}\mathrm{d}\theta, \\ y = \displaystyle\int_0^s \sin\theta\mathrm{d}s = -\int_{\theta_A}^{\theta_B}\frac{\sin\theta}{\sqrt{\dfrac{2P}{EI}\left(\cos\theta - \cos\theta_A\right)}}\mathrm{d}\theta. \end{cases} \tag{6}$$

For BC part, a fundamental equation begins with Eq. (3), and the boundary condition $\theta = 0$ at C leads to $C = P + EI(\frac{\mathrm{d}\theta}{\mathrm{d}s}|_C)^2/2$. $\frac{\mathrm{d}s}{\mathrm{d}\theta} < 0$ in BC part leads to $\mathrm{d}s = \frac{-\mathrm{d}\theta}{\sqrt{2P(1-|\cos\theta|)/EI + (\mathrm{d}\theta/\mathrm{d}s|_C)^2}}$ from Eq. (3). The length constraint of BC gives

$$\frac{\pi R}{2} = -\int_{\theta_B}^{0}\frac{1}{\sqrt{\dfrac{2P}{EI}\left(1 - |\cos\theta|\right) + \Big(\dfrac{\mathrm{d}\theta}{\mathrm{d}s}\Big|_C\Big)^2}}\mathrm{d}\theta. \tag{7}$$

The coordinates of a point in BC part can be obtained as

$$\begin{cases} x = \displaystyle -\int_{\theta_A}^{\theta_B}\frac{\cos\theta}{\sqrt{\dfrac{2P}{EI}\left(\cos\theta - \cos\theta_A\right)}}\mathrm{d}\theta - \int_{\theta_B}^{\theta}\frac{\cos\theta}{\sqrt{\dfrac{2P}{EI}\left(1 - |\cos\theta|\right) + \Big(\dfrac{\mathrm{d}\theta}{\mathrm{d}s}\Big|_C\Big)^2}}\mathrm{d}\theta, \\ y = \displaystyle -\int_{\theta_A}^{\theta_B}\frac{\sin\theta}{\sqrt{\dfrac{2P}{EI}\left(\cos\theta - \cos\theta_A\right)}}\mathrm{d}\theta - \int_{\theta_B}^{\theta}\frac{\sin\theta}{\sqrt{\dfrac{2P}{EI}\left(1 - |\cos\theta|\right) + \Big(\dfrac{\mathrm{d}\theta}{\mathrm{d}s}\Big|_C\Big)^2}}\mathrm{d}\theta. \end{cases} \tag{8}$$

The coordinates at C, i.e., x_C and y_C can thus be obtained as

$$\begin{cases} x_C = \displaystyle -\int_{\theta_A}^{\theta_B}\frac{\cos\theta}{\sqrt{\dfrac{2P}{EI}\left(\cos\theta - \cos\theta_A\right)}}\mathrm{d}\theta - \int_{\theta_B}^{0}\frac{\cos\theta}{\sqrt{\dfrac{2P}{EI}\left(1 - |\cos\theta|\right) + \Big(\dfrac{\mathrm{d}\theta}{\mathrm{d}s}\Big|_C\Big)^2}}\mathrm{d}\theta, \\ y_C = \displaystyle -\int_{\theta_A}^{\theta_B}\frac{\sin\theta}{\sqrt{\dfrac{2P}{EI}\left(\cos\theta - \cos\theta_A\right)}}\mathrm{d}\theta - \int_{\theta_B}^{0}\frac{\sin\theta}{\sqrt{\dfrac{2P}{EI}\left(1 - |\cos\theta|\right) + \Big(\dfrac{\mathrm{d}\theta}{\mathrm{d}s}\Big|_C\Big)^2}}\mathrm{d}\theta, \end{cases} \tag{9}$$

where the angle on point C remains to be zero.

At point B, the difference between two derived $\frac{\mathrm{d}\theta}{\mathrm{d}s}$ from AB part and BC part should be unchanged for the undeformed state and the compressed configuration. Recalling $\theta_B > \pi/2$, $\cos\theta_B < 0$, we obtain

$$-\sqrt{\frac{2P}{EI}(\cos\theta_B - \cos\theta_A)} + \sqrt{\frac{2P}{EI}(1+\cos\theta_B) + \Big(\frac{\mathrm{d}\theta}{\mathrm{d}s}\Big|_C\Big)^2} = \frac{1}{R}. \tag{10}$$

The following dimensionless functions are adopted:

$$\overline{R} = \sqrt{2P/(EI)}R, \quad \overline{\theta}'_C = \sqrt{EI/(2P)}\frac{\mathrm{d}\theta}{\mathrm{d}s}\Big|_C, \quad \overline{x}_C = x_C/R, \quad \overline{L} = L/R.$$

Then, the following equations can be obtained from Eqs. (5), (7), (9) and (10):

$$\begin{cases} -\displaystyle\int_{\theta_A}^{\theta_B} \frac{1}{\sqrt{\cos\theta - \cos\theta_A}}\mathrm{d}\theta = \frac{\overline{R}\,\overline{L}}{2}, \\ -\displaystyle\int_{\theta_B}^{0} \frac{1}{\sqrt{1-|\cos\theta| + \overline{\theta}'^{\,2}_C}}\mathrm{d}\theta = \frac{\pi\overline{R}}{2}, \\ -\sqrt{\cos\theta_B - \cos\theta_A} + \sqrt{(1+\cos\theta_B) + \overline{\theta}'^{\,2}_C} = \dfrac{1}{\overline{R}}, \\ \displaystyle\int_{\theta_B}^{\theta_A} \frac{\cos\theta}{\sqrt{\cos\theta - \cos\theta_A}}\mathrm{d}\theta + \int_0^{\theta_B} \frac{\cos\theta}{\sqrt{1-|\cos\theta| + \overline{\theta}'^{\,2}_C}}\mathrm{d}\theta = \overline{R}\,\overline{x}_C. \end{cases} \tag{11}$$

The integrations of the left hand side of Eq. (11) can be rewritten in the elliptic integration forms as follows:

$$\begin{cases} K\Big(\frac{\theta_A}{2}, \frac{1}{\sin\frac{\theta_A}{2}}\Big) - K\Big(\frac{\theta_B}{2}, \frac{1}{\sin\frac{\theta_A}{2}}\Big) = \dfrac{\overline{R}\,\overline{L}}{2\sqrt{2}}\sin\dfrac{\theta_A}{2}, \\ K\Big(\sqrt{\dfrac{2}{2+\overline{\theta}'^{\,2}_C}}\Big) - 2K\Big(\dfrac{\pi}{4}, \sqrt{\dfrac{2}{2+\overline{\theta}'^{\,2}_C}}\Big) + K\Big(\dfrac{\theta_B}{2}, \sqrt{\dfrac{2}{2+\overline{\theta}'^{\,2}_C}}\Big) = \dfrac{\pi\overline{R}}{4}\sqrt{2+\overline{\theta}'^{\,2}_C}, \\ -\sqrt{\cos\theta_B - \cos\theta_A} + \sqrt{\Big(1+\cos\theta_B\Big) + \overline{\theta}'^{\,2}_C} = \dfrac{1}{\overline{R}}, \\ \dfrac{\sqrt{2}\cos\theta_A}{\sin\frac{\theta_A}{2}}\Big(K\Big(\dfrac{\theta_A}{2}, \dfrac{1}{\sin\frac{\theta_A}{2}}\Big) - K\Big(\dfrac{\theta_B}{2}, \dfrac{1}{\sin\frac{\theta_A}{2}}\Big)\Big) + 2\sqrt{2}\sin\dfrac{\theta_A}{2}\Big(E\Big(\dfrac{\theta_A}{2}, \dfrac{1}{\sin\frac{\theta_A}{2}}\Big) \\ -E\Big(\dfrac{\theta_B}{2}, \dfrac{1}{\sin\frac{\theta_A}{2}}\Big)\Big) + \dfrac{2(1+\overline{\theta}'^{\,2}_C)}{\sqrt{2+\overline{\theta}'^{\,2}_C}}\Big(K\Big(\sqrt{\dfrac{2}{2+\overline{\theta}'^{\,2}_C}}\Big) - 2K\Big(\dfrac{\pi}{4}, \sqrt{\dfrac{2}{2+\overline{\theta}'^{\,2}_C}}\Big) \\ +K\Big(\dfrac{\theta_B}{2}, \sqrt{\dfrac{2}{2+\overline{\theta}'^{\,2}_C}}\Big)\Big) + 2\sqrt{(2+\overline{\theta}'^{\,2}_C)}\Big(2E\Big(\dfrac{\pi}{4}, \sqrt{\dfrac{2}{2+\overline{\theta}'^{\,2}_C}}\Big) \\ -E\Big(\sqrt{\dfrac{2}{2+\overline{\theta}'^{\,2}_C}}\Big) - 2E\Big(\dfrac{\theta_B}{2}, \sqrt{\dfrac{2}{2+\overline{\theta}'^{\,2}_C}}\Big)\Big) = \overline{R}\,\overline{x}_C, \end{cases} \tag{12}$$

where K and E are the elliptic integrations of the first kind and the second kind, defined as

$$\begin{cases} K(\phi,k)=\displaystyle\int_0^{\phi}\frac{\mathrm{d}\theta}{\sqrt{1-k^2\sin^2\theta}}, \\ K(k)=\displaystyle\int_0^{\frac{\pi}{2}}\frac{\mathrm{d}\theta}{\sqrt{1-k^2\sin^2\theta}}, \\ E(\phi,k)=\displaystyle\int_0^{\phi}\sqrt{1-k^2\sin^2\theta}\mathrm{d}\theta, \\ E(k)=\displaystyle\int_0^{\frac{\pi}{2}}\sqrt{1-k^2\sin^2\theta}\mathrm{d}\theta. \end{cases} \tag{13}$$

At a given horizontal displacement in compressing, i.e., specifying $\overline{x}_C$, one can obtain $\overline{R}$, θ_A, θ_B, and $\overline{\theta}'_C$, the coordinates of points A, B, and C via the commercial software package MATLAB.

The analytic model of the compressed nonbuckling interconnects after releasing the prestrain is obtained. Such a model with compression is regarded as the initial compressed state including the coordinates of the endpoints A, B, and C, and the geometrical shape is then used to continue the stretching process. The stretching process can be separated into two steps. The first step is during little applied stretching strain from the initial compressed state to the stress-free state. The second step is under prominent stretching, shown on the right side of Fig. 2(b).

During the first step, the stretching process is regarded as a determined process of reverse of compression which has been discussed above. For the second step, each considered parameter has been discussed in Ref. [33], and the results are given as follows.

The coordinates of AB part are

$$\begin{cases} x=\displaystyle\int_{\theta_A}^{\theta}\frac{\cos\theta}{\sqrt{\dfrac{2P}{EI}(\cos\theta_A-\cos\theta)}}\mathrm{d}\theta, \\ y=\displaystyle\int_{\theta_A}^{\theta}\frac{\sin\theta}{\sqrt{\dfrac{2P}{EI}(\cos\theta_A-\cos\theta)}}\mathrm{d}\theta. \end{cases} \tag{14}$$

The coordinates of BC part are

$$\begin{cases} x=\displaystyle\int_{\theta_A}^{\theta_B}\frac{\cos\theta}{\sqrt{\dfrac{2P}{EI}(\cos\theta_A-\cos\theta)}}\mathrm{d}\theta-\int_{\theta_B}^{\theta}\frac{\cos\theta}{\sqrt{\dfrac{2P}{EI}(1-\cos\theta)+\left(\dfrac{\mathrm{d}\theta}{\mathrm{d}s}\Big|_C\right)^2}}\mathrm{d}\theta, \\ y=\displaystyle\int_{\theta_A}^{\theta_B}\frac{\sin\theta}{\sqrt{\dfrac{2P}{EI}(\cos\theta_A-\cos\theta)}}\mathrm{d}\theta-\int_{\theta_B}^{\theta}\frac{\sin\theta}{\sqrt{\dfrac{2P}{EI}(1-\cos\theta)+\left(\dfrac{\mathrm{d}\theta}{\mathrm{d}s}\Big|_C\right)^2}}\mathrm{d}\theta. \end{cases} \tag{15}$$

The coordinates of point C are

$$\begin{cases} x_C=\displaystyle\int_{\theta_A}^{\theta_B}\frac{\cos\theta}{\sqrt{\dfrac{2P}{EI}(\cos\theta_A-\cos\theta)}}\mathrm{d}\theta-\int_{\theta_B}^{0}\frac{\cos\theta}{\sqrt{\dfrac{2P}{EI}(1-\cos\theta)+\left(\dfrac{\mathrm{d}\theta}{\mathrm{d}s}\Big|_C\right)^2}}\mathrm{d}\theta, \\ y_{\mathrm{C}}=\displaystyle\int_{\theta_A}^{\theta_B}\frac{\sin\theta}{\sqrt{\dfrac{2P}{EI}(\cos\theta_A-\cos\theta)}}\mathrm{d}\theta-\int_{\theta_B}^{0}\frac{\sin\theta}{\sqrt{\dfrac{2P}{EI}(1-\cos\theta)+\left(\dfrac{\mathrm{d}\theta}{\mathrm{d}s}\Big|_C\right)^2}}\mathrm{d}\theta. \end{cases} \tag{16}$$

The nondimensional constraint equations are

$$\begin{cases} \displaystyle\int_{\theta_A}^{\theta_B} \frac{1}{\sqrt{\cos\theta_A-\cos\theta}}\mathrm{d}\theta = \frac{\overline{R}\,\overline{L}}{2}, \\ \displaystyle-\int_{\theta_B}^{0} \frac{1}{\sqrt{1-\cos\theta+\overline{\theta}'^{\,2}_C}}\mathrm{d}\theta = \frac{\pi\overline{R}}{2}, \\ \sqrt{\cos\theta_A-\cos\theta_B}+\sqrt{(1-\cos\theta_B)+\overline{\theta}'^{\,2}_C} = \dfrac{1}{\overline{R}}, \\ \displaystyle\int_{\theta_A}^{\theta_B} \frac{\cos\theta}{\sqrt{\cos\theta_A-\cos\theta}}\mathrm{d}\theta + \int_{0}^{\theta_B} \frac{\cos\theta}{\sqrt{1-\cos\theta+\overline{\theta}'^{\,2}_C}}\mathrm{d}\theta = \overline{R}\,\overline{x}_C. \end{cases} \tag{17}$$

Similarly, the integrations of the left hand side of Eq. (17) can be rewritten in the elliptic integration forms as follows:

$$\begin{cases} K\Big(\dfrac{\pi-\theta_A}{2}, \dfrac{1}{\cos\frac{\theta_A}{2}}\Big) - K\Big(\dfrac{\pi-\theta_B}{2}, \dfrac{1}{\cos\frac{\theta_A}{2}}\Big) = \dfrac{\sqrt{2\overline{R}\,\overline{L}}}{4}\cos\dfrac{\theta_A}{2}, \\ K\Big(\sqrt{\dfrac{2}{2+\overline{\theta}'^{\,2}_C}}\Big) - K\Big(\dfrac{\pi-\theta_B}{2}, \sqrt{\dfrac{2}{2+\overline{\theta}'^{\,2}_C}}\Big) = \dfrac{\pi\overline{R}}{4}\sqrt{2+\overline{\theta}'^{\,2}_C}, \\ \sqrt{\cos\theta_A-\cos\theta_B}+\sqrt{(1-\cos\theta_B)+\overline{\theta}'^{\,2}_C} = \dfrac{1}{\overline{R}}, \\ \dfrac{\sqrt{2}\cos\theta_A}{\cos\frac{\theta_A}{2}}\Big(K\Big(\dfrac{\pi-\theta_A}{2}, \dfrac{1}{\cos\frac{\theta_A}{2}}\Big) - K\Big(\dfrac{\pi-\theta_B}{2}, \dfrac{1}{\cos\frac{\theta_A}{2}}\Big)\Big) \\ +2\sqrt{2}\cos\dfrac{\theta_A}{2}\Big(E\Big(\dfrac{\pi-\theta_B}{2}, \dfrac{1}{\cos\frac{\theta_A}{2}}\Big) - E\Big(\dfrac{\pi-\theta_A}{2}, \dfrac{1}{\cos\frac{\theta_A}{2}}\Big)\Big) \\ +\dfrac{2(1+\overline{\theta}'^{\,2}_C)}{\sqrt{2+\overline{\theta}'^{\,2}_C}}\Big(K\Big(\sqrt{\dfrac{2}{2+\overline{\theta}'^{\,2}_C}}\Big) - K\Big(\dfrac{\pi-\theta_B}{2}, \sqrt{\dfrac{2}{2+\overline{\theta}'^{\,2}_C}}\Big)\Big) \\ +2\sqrt{(2+\overline{\theta}'^{\,2}_C)}\Big(E\Big(\dfrac{\pi-\theta_B}{2}, \sqrt{\dfrac{2}{2+\overline{\theta}'^{\,2}_C}}\Big) - E\Big(\sqrt{\dfrac{2}{2+\overline{\theta}'^{\,2}_C}}\Big)\Big) = \overline{R}\,\overline{x}_C, \end{cases} \tag{18}$$

where K and E are the elliptic integrations of the first kind and the second kind, respectively. For a serpentine structure, the local maximum strain defined as $\varepsilon_{\max}$, is reached at C. It is described as

$$\varepsilon_{\max} = \frac{1}{2}\kappa w = \frac{w}{2}\left|\Big(\Big(\frac{\mathrm{d}\theta}{\mathrm{d}s}\Big|_C\Big) + \frac{1}{R}\Big)\right|. \tag{19}$$

For the compressed configuration (shown in the middle of Fig. 2(b), $\big(\frac{\mathrm{d}\theta}{\mathrm{d}s}\big)|_C < -1/R$, Eq. (19) can be deduced as

$$\varepsilon_{\max} = -\frac{w}{2}\Big(\Big(\frac{\mathrm{d}\theta}{\mathrm{d}s}\Big|_C\Big) + \frac{1}{R}\Big). \tag{20}$$

For the stretched configuration shown on the right hand side of Fig. 2(b), $-1/R < \big(\frac{\mathrm{d}\theta}{\mathrm{d}s}\big)|_C < 0$, Eq. (19) is deduced as

$$\varepsilon_{\max} = \frac{w}{2}\Big(\Big(\frac{\mathrm{d}\theta}{\mathrm{d}s}\Big|_C\Big) + \frac{1}{R}\Big). \tag{21}$$

The nondimensional maximum strain $(R/w)\,\varepsilon_{\max}$ is obtained, which can donate the local maximum strain of the quarter period, i.e., also the global maximum strain of a periodic serpentine structure. Notably, $(R/w)\,\varepsilon_{\max}$ remaining to be zero means a stress-free state, and a large $(R/w)\,\varepsilon_{\max}$ means a significant change of configuration. Since for a nonbuckling serpentine structure discussed above, the maximum strain is reached at the arc peak. For the compressed configuration, the curvature of the arc peak increases with increasing $(R/w)\,\varepsilon_{\max}$ according to Eq. (20). For the stretched configuration, the curvature of the arc peak decreases with increasing $(R/w)\,\varepsilon_{\max}$ according to Eq. (21).

The analytic results at several stages of deformation are shown in Fig. 2(c), and the numerical results are shown by red spots simultaneously. In order to find regularity, the analytic and numerical studies on mechanical behaviors are based on the elastic theory. The influence of the substrate is not discussed here. Instead, a compressed nonbuckling interconnect after releasing the prestrain of substrate is modeled as such serpentine structure subjected to concentrate loading force in finite element simulation. Due to the above assumption, a compression level is introduced as $\varepsilon_{\text{pre-compression}} = l_{\text{compression}}/l_{\text{original-length}}$ to evaluate the compression and reflect the level of prestrain, where $l_{\text{compression}}$ is the length of compression in the x-direction, and $l_{\text{original-length}}$ is the length of nonbuckling interconnect in the undeformed state (R for quarter period structure). The applied strain is defined as $\varepsilon_{\text{applied}} = l_{\text{elongation}}/l_{\text{compressed-length}}$ during the stretching process, where $l_{\text{elongation}}$ is the elongation of interconnects along the stretching direction, and $l_{\text{compressed-length}}$ is the length of the compressed nonbuckling interconnect in the initial compressed state.

Due to symmetry, only a half period of the interconnect with arc radius $R = 0.25$ mm, thickness $t = 0.05$ mm, width $w = 0.05$ mm, and straight segment length $L = 1$ mm, has been analyzed in the commercial software package ABAQUS, with displacement loading applied in the direction of compression or stretching. The 4-node doubly curved thick shell element is adopted for the interconnect, which is described by a linear elastic material with Young's modulus 124 GPa and Poisson's ratio 0.34. The undeformed configuration is shown on the top of the Fig. 2(c). The following second subfigure shows the deformed configuration with 18% compression and none applied strain (the maximum strain of the interconnects reaches 0.3% for the half of the cross section of the end C). The FEA result shows that the interconnects produce in-plane bending deformation with increasing arc curvature of curvilinear segments and incline with the decreasing spacing between the adjacent straight segments. During the stretching process, the nonbuckling interconnects first recover to the stress-free state, i.e., its undeformed configuration (shown in Fig. 2(c), the third subfigure) with 22% applied strain. During the following stretching process, the FEA result shows in-plane deformation of the nonbuckling interconnects, with the decreasing curvature of curvilinear segments and increasing spacing between inclined straight segments (shown in Fig. 2c, the last subfigure). During the whole deformation period, the accuracy of the analytic results is confirmed by perfect agreement with the FEA.

3 Effects of levels of prestrain and interconnects constructed using various layouts

This section summarizes the effects of different levels of prestrain and geometric parameters on the non-dimensional maximum strains of the serpentine interconnect. The curves of the analytic nondimensional maximum strain versus the applied strain with different levels of pre-compression are shown in Fig. 3(a) for $\overline{L} = 10$. Compared with non-prestrained samples, the prestrained interconnects show a decreasing nondimensional maximum strain during the incipient stretching process. At the point of nondimensional maximum strain reaching zero, the interconnects recover to the stress-free state. During the following stretching process, nondimensional maximum strain increases monotonically. This tendency demonstrates well on the

enhancement of stretchability for nonbulcking interconnect with prestrain. Figure 3(b) shows that for a specific applied strain, the analytic maximum strain decreases with increasing the pre-compression level. The curves of analytic maximum strain versus nondimensional $\overline{L}$ are exhibited in Fig. 3(c) for different pre-compression levels when $\varepsilon_{\text{applied}} = 0$. It can be found that a large pre-compression causes a large strain at the initial compressed state, and increasing $\overline{L}$ can significantly reduce the maximum strain of the interconnects. Figure 3(d) illustrates that for a large applied strain, increasing pre-compression and $\overline{L}$ can significantly reduce the maximum strain.

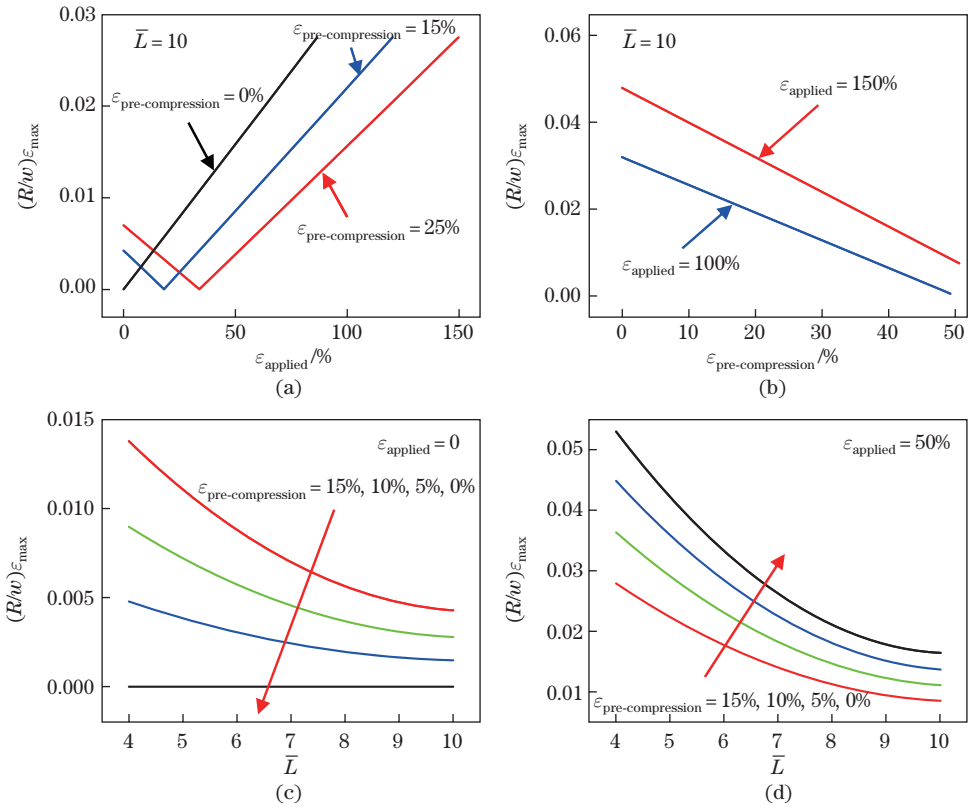

Fig. 3 (a) Curves of analytic nondimensional maximum strains versus applied strain with different sets of pre-compression for interconnects with $\overline{L} = 10$. (b) Curves of analytic nondimensional maximum strains versus pre-compression with 100% applied strain and 150% applied strain for interconnects with $\overline{L} = 10$. Curves of analytic nondimensional maximum strains versus $\overline{L}$ with 0%, 5%, 10% and 15% pre-compression for cases of (c) 0% applied strain and (d) 50% applied strain (color online)

The encapsulation is used in practical design, where the interconnects are bonded to the substrate. In contrast to the situation without substrate in Fig. 2(c), the FEA illustrates the effects of substrate with 22% prestrain in Fig. 4(a). The compression level of interconnects is consistent with Fig. 2(c) according to $\varepsilon_{\text{pre-compression}} = \varepsilon_{\text{prestrain}}/(1+\varepsilon_{\text{prestrain}})$. The 8-node linear brick element is adopted for the elastic substrate that is regarded as a hyperelastic material as described by the Mooney-Rivlin model, with $C_{10} = 0.008\ 054$ MPa, $C_{01} = 0.002\ 013$ MPa, and $D_1 = 2.0\ \text{MPa}^{-1}$. The on-top subfigure in Fig. 4(a) shows the configuration of the interconnects bonded to the substrate before releasing the prestrain. The second subfigure shows the compressed configuration after releasing the prestrain. The FEA result shows that the interconnects produce in-plane bending deformation with increasing the arc curvature of curvilinear

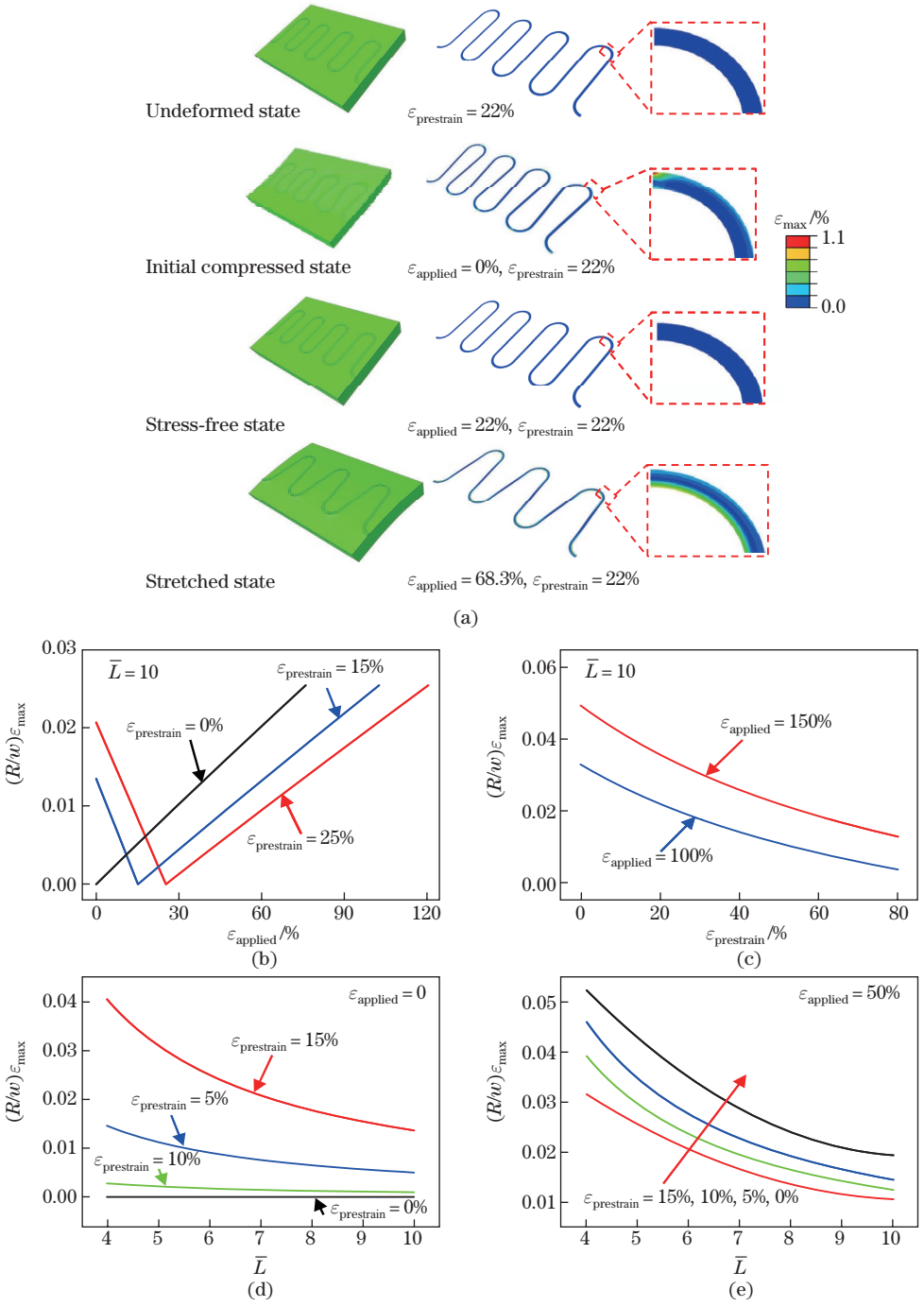

Fig. 4 (a) Configurations of FEA results for interconnects with substrate and corresponding distribution of maximum principal strain. (b) Curves of nondimensional maximum strains versus applied strain with different levels of prestrain for interconnects with $\overline{L} = 10$. (c) Curves of nondimensional maximum strains versus prestrain with 100% applied strain and 150% applied strain for interconnects with $\overline{L} = 10$. Curves of nondimensional maximum strains versus $\overline{L}$ with 0%, 5%, 10% and 15% prestrain for cases of (d) 0% applied strain and (e) 50% applied strain (color online)

segments and incline with the decreasing spacing between the adjacent straight segments. This result shows a significant difference from out-of-plane buckling of thin structures[32], where thin ribbon Cu produces both in- and out-plane buckling deformations and straight segments get closer and keep nearly vertical. The FEA result on the right hand side shows that the maximum strain in the interconnects is slightly greater than that in the interconnects without substrate. It is because the constraint from the substrate restricts the free motion of the interconnect, which yields large strain early at the arc peak and leads to local strain concentration. Due to elastic deformation, the interconnects still recover to the stress-free state during the stretching process. The in-plane bending deformation, predicted by the FEA, is produced in the interconnects with the increasing applied strain. The curvature of the curvilinear segment decreases and the straight segments incline with the increasing spacing (shown in the bottom subfigure of Fig. 4(a)).

The effects of different parameters on the maximum strain during the nonbuckling deformation of the interconnects with prestrained substrate are studied numerically. The trends of FEA results are consistent with those of analytic results. In Fig. 4(b), compared with the non-prestrain sample, the nondimensional maximum strain of the nonbuckling interconnect with prestrain goes through a decreasing stage at the beginning of stretching. An increasing prestrain level correspondingly extends the decreasing stage during the stretching process. For a large applied strain, a large level prestrain of the substrate can effectively reduce the maximum strain in the nonbuckling interconnects, shown in Fig. 4(c). However, on the other hand, Fig. 4(d) also illustrates that for different $\overline{L}$, increasing prestrain induces an increasing maximum strain in the initial compressed state ($\varepsilon_{\text{applied}} = 0$), which means a potential constraint of the prestrain to the substrate. Consist with the analytic model discussed above, Fig. 4(e) shows that increasing prestrain level and $\overline{L}$ can effectively reduce the maximum strain in the nonbuckling interconnect, thus improving its stretchability.

4 Concluding remarks

(i) The prestrain design enhances the stretchability of nonbuckling interconnects, which produce in-plane nonbuckling deformation after releasing the prestrain of the substrate and under the stretching of the substrate.

(ii) An analytic model for finite deformation problem of nonbuckling serpentine interconnects design with prestrain is developed. Accurate deformation configurations after releasing the prestrain and under the stretching to the serpentine interconnects are obtained.

(iii) For nonbuckling interconnect design with prestrain-released substrate, large levels of prestrain induce small maximum strain of the nonbuckling interconnects under stretching, thus enhancing the stretchability. On the other hand, a large prestrain also yields a large maximum strain after releasing the prestrain, which means a constraint of the prestrain to the substrate.

(iv) The stretchability is highly influenced by structural design, i.e., long straight segments and small arc radii for nonbuckling interconnects yield lower strain in the interconnect, thus enhancing the stretchability.

References

[1] SUGIMOTO, A., OCHI, H., FUJIMURA, S., YOSHIDA, A., MIYADERA, T., and TSUCHIDA, M. Flexible OLED displays using plastic substrates. *IEEE Journal of Selected Topics in Quantum*

Electronics, **10**(1), 107–114 (2004)

[2] CRAWFORD, G. P. *Flexible Flat Panel Display Technology*, Wiley Online Library, New York (2005)

[3] KIM, S., KWON, H. J., LEE, S., SHIM, H., CHUN, Y., CHOI, W., KWACK, J., HAN, D., SONG, M., and KIM, S. Low-power flexible organic light-emitting diode display device. *Advanced Materials*, **23**(31), 3511–3516 (2011)

[4] DAGDEVIREN, C., YANG, B. D., SU, Y., TRAN, P. L., JOE, P., ANDERSON, E., XIA, J., DORAISWAMY, V., DEHDASHTI, B., and FENG, X. Conformal piezoelectric energy harvesting and storage from motions of the heart, lung, and diaphragm. *Proceedings of the National Academy of Sciences*, **111**(5), 1927–1932 (2014)

[5] HATTORI, Y., FALGOUT, L., LEE, W., JUNG, S. Y., POON, E., LEE, J. W., NA, I., GEISLER, A., SADHWANI, D., and ZHANG, Y. Multifunctional skin-like electronics for quantitative, clinical monitoring of cutaneous wound healing. *Advanced Healthcare Materials*, **3**(10), 1597–1607 (2014)

[6] XU, S., ZHANG, Y., CHO, J., LEE, J., HUANG, X., JIA, L., FAN, J. A., SU, Y., SU, J., and ZHANG, H. Stretchable batteries with self-similar serpentine interconnects and integrated wireless recharging systems. *Nature Communication*, **4**(1), 1–8 (2013)

[7] KO, H. C., STOYKOVICH, M. P., SONG, J. Z., MALYARCHUK, V., CHOI, W. M., YU, C. J., GEDDES, J. B., XIAO, J. L., WANG, S. D., HUANG, Y. G., and ROGERS, J. A. A hemispherical electronic eye camera based on compressible silicon optoelectronics. *nature*, **454**(7205), 748–753 (2008)

[8] MENGÜÇ, Y., YANG, S. Y., KIM, S., ROGERS, J. A., and SITTI, M. Gecko-inspired controllable adhesive structures applied to micromanipulation. *Advanced Functional Materials*, **22**(6), 1246–1254 (2012)

[9] KIM, D. H., LU, N., MA, R., KIM, Y. S., KIM, R. H., WANG, S., WU, J., WON, S. M., TAO, H., and ISLAM, A. Epidermal electronics. *Science*, **333**(6044), 838–843 (2011)

[10] ZENG, W., SHU, L., LI, Q., CHEN, S., WANG, F., and TAO, X. M. Fiber-based wearable electronics: a review of materials, fabrication, devices, and applications. *Advanced Materials*, **26**(31), 5310–5336 (2014)

[11] WON, S. M., SONG, E. M., REEDER, J. T., and ROGERS, J. A. Emerging modalities and implantable technologies for neuromodulation. *Cell*, **181**(1), 115–135 (2020)

[12] KHANG, D. Y., JIANG, H. Q., HUANG, Y., and ROGERS, J. A. A stretchable form of single-crystal silicon for high-performance electronics on rubber substrates. *Science*, **311**(5758), 208–212 (2006)

[13] ZHANG, Y. and HUANG, Y. Assembly of micro/nanomaterials into complex, three-dimensional architectures by compressive buckling. *The 6th International Conference on Nanoscience and Technology*, **347**(6218), 154–159 (2015)

[14] SU, Y. W., LIU, Z. J., KIM, S., WU, J., HUANG, Y. G., and ROGERS, J. A. Mechanics of stretchable electronics with high fill factors. *International Journal of Solids*, **49**(23-24), 3416–3421 (2012)

[15] ROGERS, J. A., SOMEYA, T., and HUANG, Y. G. Materials and mechanics for stretchable electronics. *Science*, **327**(5973), 1603–1607 (2010)

[16] HWANG, S. W., TAO, H., KIM, D. H., CHENG, H. Y., SONG, J. K., RILL, E., BRENCKLE, M. A., PANILAITIS, B., WON, S. W., KIM, Y. S., SONG, Y. M., YU, K. J., AMEEN, A., LI, R., SU, Y. W., YANG, M. M., KAPLAN, D. L., ZAKIN, M. R., SLEPIAN, M. J., HUANG, Y. G., OMENTTO, F. G., and ROGERS, J. A. A physically transient form of silicon electronics. *Science*, **337**(6102), 1640–1644 (2012)

[17] BOWDEN, N., BRITTAIN, S., EVANS, A. G., HUTCHINSON, J. W., and WHITESIDES, G. M. Spontaneous formation of ordered structures in thin films of metals supported on an elastomeric polymer. *nature*, **393**(6681), 146–149 (1998)

[18] CHOI, W. M., SONG, J. Z., KHANG, D. Y., JIANG, H. Q., HUANG, Y. Y., and ROGERS, J. A. Biaxially stretchable "wavy" silicon nanomembranes. *Nano Letters*, **7**(6), 1655–1663 (2007)

[19] LACOUR, S. P., JONES, J., WAGNER, S., LI, T., and SUO, Z. G. Stretchable interconnects for elastic electronic surfaces. *Proceedings of the IEEE*, **93**(8), 1459–1467 (2005)

[20] LEE, J., WU, J., SHI, M. X., YOON, J., PARK, S. I., LI, M., LIU, Z. G., HUANG, Y. G., and ROGERS, J. A. Stretchable solar cells: stretchable GaAs photovoltaics with designs that enable high areal coverage. *Advanced Materials*, **23**, 986–991 (2011)

[21] KIM, D. H., SONG, J., CHOI, W. M., KIM, H. S., KIM, R. H., LIU, Z. J., HUANG, Y. G., HWANG, K. C., ZHANG, Y. W., and ROGERS, J. A. Materials and noncoplanar mesh designs for integrated circuits with linear elastic responses to extreme mechanical deformations. *Proceedings of the National Academy of Sciences*, **105**(48), 18675–18680 (2008)

[22] SONG, J. Z., FENG, X., and HUANG, Y. G. Mechanics and thermal management of stretchable inorganic electronics. *National Science Review*, **3**(1), 128–143 (2016)

[23] KIM, D. H., LU, N. S., HUANG, Y. G., and ROGERS, J. A. Materials for stretchable electronics in bioinspired and biointegrated devices. *MRS Bulletin*, **37**(3), 226–235 (2012)

[24] XU, S., ZHANG, Y. H., JIA, L., MATHEWSON, K. E., JANG, K. I., KIM, J. H., FU, H. R., HUANG, X., CHAVA, P., WANG, R. H., BHOLE, S., WANG, L. Z., NA, Y. J., GUAN, Y., FLAVIN, M., HAN, Z. S., HUANG, Y. G., and ROGERS, J. A. Soft microfluidic assemblies of sensors, circuits, and radios for the skin. *Science*, **344**(6179), 70–74 (2014)

[25] WANG, A., AVILA, R., and MA, Y. J. Mechanics design for buckling of thin ribbons on an elastomeric substrate without material failure. *Journal of Applied Mechanics*, **84**(9), 094501 (2017)

[26] FAN, J. A., YEO, W. H., SU, Y., HATTORI, Y., LEE, W., JUNG, S. Y., ZHANG, Y., LIU, Z., CHENG, H., and FALGOUT, L. Fractal design concepts for stretchable electronics. *Nature Communication*, **5**(1), 1–8 (2014)

[27] SU, Y. W., WANG, S. D., HUANG, Y., LUAN, H. W., DONG, W. T., FAN, J. A., YANG, Q. L., ROGERS, J. A., and HUANG, Y. G. Elasticity of fractal inspired interconnects. *Small*, **11**(3), 367–373 (2015)

[28] XU, S., YAN, Z., JANG, K. I., HUANG, W., FU, H., KIM, J., WEI, Z., FLAVIN, M., MCCRACKEN, J., and WANG, R. Assembly of micro/nanomaterials into complex, three-dimensional architectures by compressive buckling. *Science*, **347**(6218), 154–159 (2015)

[29] SU, Y., PING, X., YU, K. J., LEE, J. W., FAN, J. A., WANG, B., LI, M., LI, R., HARBURG, D. V., and HUANG, Y. In-plane deformation mechanics for highly stretchable electronics. *Advanced Materials*, **29**(8), 1604989 (2017)

[30] LI, M., LI, X., CHE, L. X., LI, F. W., and KANG, Z. Non-uniform global-buckling and local-folding in thin film of stretchable electronics. *International Journal of Mechanical Sciences*, **175**, 105537 (2020)

[31] ZHANG, Y. C., JIAO, Y., WU, J., MA, Y. J., and FENG, X. Configurations evolution of a buckled ribbon in response to out-of-plane loading. *Extreme Mechanics Letters*, **34**, 100604 (2020)

[32] ZHANG, Y. H., WANG, S. D., LI, X. T., FAN, J. A., XU, S., SONG, Y. M., CHOI, K. J., YEO, W. H., LEE, W., and NAZAAR, S. N. Experimental and theoretical studies of serpentine microstructures bonded to prestrained elastomers for stretchable electronics. *Advanced Functional Materials*, **24**(14), 2028–2037 (2014)

[33] LIU, H., XUE, R. Y., HU, J. Q., PING, X. C., WU, H. D., HUANG, M. Q., ZHANG, H., GUO, X., LI, R., CHEN, Y. L., and SU, Y. W. Systematic study on the mechanical and electric behaviors of the nonbuckling interconnect design of stretchable electronics. *Science China Physics, Mechanics & Astronomy*, **61**(11), 114611 (2018)

[34] TIMOSHENKO, S. and GERE, J. M. *Theory of Elastic Stability*, McGraw Hill, New York (1961)